

# INTERPRETATION OF MAGNETIC ANOMALY PROFILES USING A DECOMPOSITION IN HILBERT TRANSFORM PAIRS

Saulo Pomponet Oliveira <sup>1\*</sup>, Jeferson de Souza <sup>2</sup>,  
Luis Gustavo de Castro <sup>1</sup>, and Francisco José Fonseca Ferreira <sup>1</sup>

<sup>1</sup>Universidade Federal do Paraná - UFPR, Centro Politécnico, Curitiba, PR, Brazil

<sup>2</sup>Secretaria de Estado da Educação do Paraná, Curitiba, PR, Brazil

\*Corresponding author: [saulopo@ufpr.br](mailto:saulopo@ufpr.br)

**ABSTRACT.** We propose a simple transformation to aid the interpretation of magnetic anomalies generated by linear structures. The profile of such anomalies perpendicular to the strike can be decomposed into two signals, one symmetric and the other antisymmetric concerning the center of the source. The symmetric component serves as input data to various depth estimation techniques that often assume the anomaly is reduced to the pole. We use the fact that these components form a Hilbert transform pair to transform a skewed anomaly profile into a symmetric one. Unlike in previous works that rely on the decomposition into even and odd functions, the profile does not need to be shifted to the source's center of symmetry or limited to one isolated anomaly. Multiple effective magnetization directions presented by different dikes are modeled by a function representing the different local effective dip angles. We validate the method with synthetic data and ground magnetic survey data from a dike swarm in Ponta Grossa Arch, southern Brazil. We also illustrate the usefulness of reconstructed anomalies for depth estimation methods. The results also show that the method can handle interfering sources with distinct effective magnetization directions.

**Keywords:** potential methods, magnetics, Hilbert transform, remanent magnetization.

## INTRODUCTION

The seminal work of Nabighian (1972) on the analysis of two-dimensional structures with the analytic signal is the starting point of numerous enhancement and depth estimation techniques for magnetic data (Roest et al., 1992; Debeglia and Corgel, 1997; Bastani and Pedersen, 2001; Cooper, 2014, to name a few).

The magnetic anomaly profile of a dike model of infinite depth to the bottom, as well as other 2D structures, can be mathematically expressed in form  $f(x) = A[\cos Qf^s(x) + \sin Qf^a(x)]$ , where  $A$  is an amplitude coefficient and  $Q$  is an effective angle that depends on geological and magnetic dips. At the same time,  $f^s(x)$  and  $f^a(x)$  are composite functions of inverse tangents and logarithms, respectively (Nabighian, 1972). The use of the analytic signal to interpret magnetic data was motivated by the fact that horizontal and vertical derivatives of  $f(x)$  constitute a Hilbert transform pair. The Hilbert transform

is a standard interpretation tool (Shuey, 1972; Mohan et al., 1982; Ram Babu and Atchuta Rao, 1991). On the other hand, the fact that  $f^s(x)$  and  $f^a(x)$  also constitute a Hilbert transform pair has yet to be well explored in the literature, to our knowledge.

Hutchison (1958) pioneered the decomposition of magnetic profiles into  $f^s(x)$  and  $f^a(x)$ , studying their symmetry properties and determining source parameters from their representation in logarithmic scale. In particular,  $f^s(x)$  and  $f^a(x)$  become respectively even and odd functions when the origin is shifted to the source center. He also pointed out that these components can be separated by a graphical procedure later formalized as a decomposition into even and odd functions (Rao and Murthy, 1967), while the location of the symmetry centers was studied by Powell (1967). Naudy (1971) used a local decomposition version to locate symmetry centers. Bhimasankaram et al. (1978) applied this parity decomposition to obtain the depth, half-width, and effective angle  $Q$  in the

frequency domain. Kara et al. (2017) further developed several interpretation tools from the same principle. de Souza et al. (2020) proposed a weighted average based on both even and odd components as an alternative to the reduction-to-the-pole filter.

We use the relationship between  $f^s(x)$  and  $f^a(x)$  based on Hilbert transform to obtain a reconstructed symmetric anomaly without having to displace the origin of the coordinate system to the dike's center. This approach can generalize the above studies to the case of multiple dikes and other two-dimensional structures. As de Souza et al. (2020) pointed out, the reconstructed anomaly allows the use of depth estimation techniques developed for anomalies with vertical magnetization (e.g., Phillips et al., 2007; Salem et al., 2007; Oliveira et al., 2017). Similarly to Paine et al. (2001) and Pilkington and Beiki (2013), the reconstruction algorithm can be employed in an inversion code to reduce the influence of remanent magnetism.

## THEORY AND METHODS

Let us initially consider the following model of a magnetic anomaly due to a single dike centered at  $x_0$  (McGrath and Hood, 1970; de Souza et al., 2020)

$$f(x) = \cos Q A f^s(x) + \sin Q A f^a(x), \quad (1)$$

$$f^s(x) = \tan^{-1} \frac{x - x_0 + a}{z_0} - \tan^{-1} \frac{x - x_0 - a}{z_0}, \quad (2)$$

$$f^a(x) = \frac{1}{2} \ln \frac{(x - x_0 + a)^2 + z_0^2}{(x - x_0 - a)^2 + z_0^2}. \quad (3)$$

The  $x$  axis is perpendicular to the strike of the dike. The model parameters are as follows:  $a$  is the half-width,  $z_0$  is the depth to the top of the dike from the plane of observation,  $A$  is the amplitude factor, and  $Q$  is the effective dip angle. A similar formula applies to finite steps (Nabighian, 1972; Ram Babu and Atchuta Rao, 1991). Parameters  $A$  and  $Q$  are given as follows:

$$A = 2Jbc \sin \theta, \quad \begin{cases} b^2 = \sin^2 i + \cos^2 i \cos^2 d, \\ c^2 = \sin^2 I + \cos^2 I \cos^2 D, \end{cases} \quad (4)$$

$$Q = \lambda + \psi - \theta - 90^\circ, \quad \begin{cases} \tan \psi = \tan i / \cos d, \\ \tan \lambda = \tan I / \cos D, \end{cases} \quad (5)$$

where  $J$  is the total magnetization intensity and  $\theta$  is the geologic dip angle, while  $(i, d)$  and  $(I, D)$  are the inclination and declination of the resultant magnetization and the earth's magnetic field, respectively (see Figure 1 – McGrath and Hood, 1970, – for a comprehensive view of these parameters).

The dikes' parameters provide valuable information for groundwater and hydrocarbon exploration and crustal evolution studies. For example, the same tectonic event may have generated dikes with similar effective dip angle  $Q$ . In addition, the relative crustal extension can be estimated by calculating the sum of

the dikes' widths from a profile taken perpendicularly to the dike swarm divided by the total profile length (Castro et al., 2008). On the other hand, width and depth to the top can affect the circulation and flow of groundwater and hydrocarbon in several ways, such as compartmentalization, obstruction, and preferential pathways development (Cavalcante et al., 2020). As McGrath and Hood (1970) pointed out, the depth to the top  $z_0$  can be estimated independently on geological or magnetization directions assuming the dike model. This allows a preliminary quantitative interpretation of gravity or magnetic data.

Superscripts  $s$  and  $a$  in functions  $f^s$  and  $f^a$  are employed to indicate that these functions are respectively symmetric and antisymmetric concerning  $x_0$ , i.e.,  $f(x_0 - x) = f(x_0 + x)$  and  $f(x_0 - x) = -f(x_0 + x)$ . When  $x_0 = 0$ , symmetric and antisymmetric functions become even and odd, i.e.,  $f(-x) = f(x)$  and  $f(-x) = -f(x)$  respectively (de Souza et al., 2020).

As pointed out by Ram Babu and Atchuta Rao (1991), the Hilbert transform of  $f(x)$  when  $x_0 = 0$  is  $H[f(x)] = -\cos Q A f^a(x) + \sin Q A f^s(x)$ , thus  $H[f^s(x)] = -f^a(x)$  and  $H[f^a(x)] = f^s(x)$ , i.e.,  $f^s$  and  $f^a$  constitute a Hilbert transform pair. Because the Hilbert transform is shift-invariant,  $f^s$  and  $f^a$  are a Hilbert transform pair also when  $x_0 \neq 0$ . It follows that the anomaly  $f(x)$  and its symmetric component  $Af^s(x)$  satisfy

$$\begin{cases} f(x) = \cos Q A f^s(x) - \sin Q H[Af^s(x)], \\ H[f(x)] = \cos Q H[Af^s(x)] + \sin Q A f^s(x). \end{cases} \quad (6)$$

In matrix form, we have

$$\begin{bmatrix} f(x) \\ H[f(x)] \end{bmatrix} = \begin{bmatrix} \cos Q & -\sin Q \\ \sin Q & \cos Q \end{bmatrix} \begin{bmatrix} Af^s(x) \\ H[Af^s(x)] \end{bmatrix}. \quad (7)$$

Solving the above system for  $[Af^s(x), H[Af^s(x)]]^T$ , we find

$$\begin{bmatrix} Af^s(x) \\ H[Af^s(x)] \end{bmatrix} = \begin{bmatrix} \cos Q & \sin Q \\ -\sin Q & \cos Q \end{bmatrix} \begin{bmatrix} f(x) \\ H[f(x)] \end{bmatrix}. \quad (8)$$

Note that the components of the zero-order analytic signal (Cooper, 2015) of  $f(x)$  and  $Af^s(x)$  are related by a classical rotation matrix with angle  $Q$ , which does not change the amplitude of the rotated signal, hence the transformation from  $f(x)$  to  $Af^s(x)$  is energy-preserving.

The symmetric anomaly  $Af^s(x)$  can be obtained from the first row in Equation 8:

$$Af^s(x) = \cos Q f(x) + \sin Q H[f(x)], \quad (9)$$

noting that the Hilbert transform can be readily computed in Fourier space (Nabighian, 1972). We remark that the inverse rotation matrix in Equation 8 is merely a transposition that does not involve di-

vision by  $\sin Q$  or  $\cos Q$ , hence Equation 9 does not involve division by these terms as in Equation 12 of de Souza et al. (2020), where an ad-hoc weighting factor  $w = |\cos Q|$  is necessary to avoid instability when  $Q = 0^\circ$  or  $Q = 90^\circ$ . Moreover, the same procedure can be applied to the spatial derivatives of the total field anomaly, since the derivatives of  $f^s$  and  $f^a$  are also Hilbert transform pairs.

The case of multiple dikes can be handled similarly. Let us consider

$$f(x) = \sum_{i=0}^n f_i(x), \tag{10}$$

$$f_i(x) = \cos Q_i A_i f_i^s(x) + \sin Q_i A_i f_i^a(x),$$

where functions  $f_i^s$  and  $f_i^a$  are defined analogously as in Equations 2 and 3:

$$f_i^s(x) = \tan^{-1} \frac{x - x_{0,i} + a_i}{z_{0,i}} - \tan^{-1} \frac{x - x_{0,i} - a_i}{z_{0,i}}, \tag{11}$$

$$f_i^a(x) = \frac{1}{2} \ln \frac{(x - x_{0,i} + a_i)^2 + z_{0,i}^2}{(x - x_{0,i} - a_i)^2 + z_{0,i}^2}. \tag{12}$$

Since Equation 9 holds for each anomaly  $f_i$ , we have from the superposition principle that the sum of their symmetric components satisfies

$$\sum_{i=0}^n A_i f_i^s(x) = \sum_{i=0}^n \cos Q_i f_i(x) + \sin Q_i H[f_i(x)]. \tag{13}$$

Similarly as de Souza et al. (2020), we refer to the symmetric profile defined by the left-hand side of Equation 13 as the reconstructed profile, and denote it as  $f^{rec}$ . In practice, we cannot obtain  $f^{rec}$  from Equation 13 because the individual anomalies  $f_i$  are unknown.

We consider two approaches to approximately compute  $f^{rec}$ . The first approach is intended to the case of low variation of the effective dip angle: if  $Q_i \approx Q$ , then Equation 13 reduces to

$$\begin{aligned} f^{rec}(x) &= \cos Q \sum_{i=0}^n f_i(x) + \sin Q H \left[ \sum_{i=0}^n f_i(x) \right] \\ &= \cos Q f(x) + \sin Q H[f(x)], \end{aligned} \tag{14}$$

thus coinciding with the formula for a single anomaly, Equation 9. The second approach divides the profile in intervals  $[a_j, b_j]$  where we assume  $f_i(x) \approx 0$  for  $i \neq j$ , i.e.,  $f_j(x) \approx f(x)$  within this interval. In this case,

$$f^{rec}(x) = \cos Q_j f(x) + \sin Q_j H[f(x)] \text{ for } x \in [a_j, b_j]. \tag{15}$$

Since  $H[f_z] = f_x$  and  $H[f_x] = -f_z$ , we have the following expressions for the reconstructed par-

tial derivatives:

$$f_z^{rec}(x) = \cos Q_j f_z(x) + \sin Q_j f_x(x) \text{ for } x \in [a_j, b_j], \tag{16}$$

$$f_x^{rec}(x) = \cos Q_j f_x(x) - \sin Q_j f_z(x) \text{ for } x \in [a_j, b_j]. \tag{17}$$

We define the intervals  $[a_j, b_j]$  using the local minima of the tilt angle of the zero-order analytic signal amplitude (Cooper, 2014):

$$\text{TAS}_0 = \tan^{-1} \frac{\partial \text{AS}_0 / \partial z}{|\partial \text{AS}_0 / \partial x|}, \quad \text{AS}_0 = \sqrt{f^2 + H[f]^2}. \tag{18}$$

Similarly as in Cooper and Cowan (2006), approximating the vertical derivative of  $\text{AS}_0$  in the frequency domain provides better results than its analytical expression

$$\frac{\partial \text{AS}_0}{\partial z} = \frac{f_z f + H[f_z] H[f]}{\text{AS}_0}. \tag{19}$$

Filter  $\text{TAS}_0$  combines the low sensitivity of the analytical signal amplitude to the effective dip angles  $Q_j$  with the amplitude equalization of shallow and deep sources provided by the tilt angle.

The approximation provided by Equation 15 neglects the influence of adjacent dikes, producing discontinuities between intervals. To mitigate unaccounted interference, we adjust the base level of  $f^{rec}$  at each interval to the average value of the entire reconstructed profile.

The approaches represented by Equations 14 and 15 require estimates of effective dip angles. We employed the selection criterion proposed by Danne-miller and Li (2006), i.e., we selected the angle  $Q$  (or  $Q_j$ ) that maximizes the correlation between vertical derivative and analytical signal amplitude, i.e.,

$$C(Q_{est}) = \min_Q C(Q), \tag{20}$$

where the correlation function is

$$C(Q) = \frac{\sum_j (v_j - \bar{v})(t_j - \bar{t})}{\sqrt{\sum_j (v_j - \bar{v})^2 \sum_j (t_j - \bar{t})^2}}, \tag{21}$$

and  $v_j = f_z^{rec}(x_j)$ ,  $t_j = \sqrt{(f_x^{rec}(x_j))^2 + (f_z^{rec}(x_j))^2}$  for each point  $x_j$ , while  $\bar{v}$  and  $\bar{t}$  are their mean values. To obtain the estimates for  $Q_j$ , we constrain  $x_j$  to the interval  $[a_j, b_j]$  as in Equation 15.

We illustrate the use of the reconstructed profiles to estimate depth of the dikes using, for comparison, the Signum-transform method (de Souza and Ferreira, 2012; Weihermann et al., 2018) and Euler deconvolution (Thompson, 1982). In the Signum-transform method, the depth to the top  $z_0$  is estimated as follows:

$$z_0 = \frac{x_v^2 - x_{vh}^2}{2x_{vh}}, \tag{22}$$

where  $x_v$  and  $x_{vh}$  are half of the interval lengths where

the Signum transforms of  $f_z$  and  $f_z - |f_x|$  are positive, respectively. The Signum transform of a function  $g(x)$  is defined as

$$ST[g(x)] = \begin{cases} g(x)/|g(x)|, & g(x) \neq 0, \\ 1, & g(x) = 0. \end{cases} \quad (23)$$

As the Signum-transform method assumes the effective dip angle  $Q = 0$ , we approximate the field derivatives by the reconstructed profiles of  $f_x$  and  $f_z$ . We compute  $x_v$  and  $x_{vh}$  using the algorithm EdgeDetectPFI (Oliveira et al., 2017).

Euler deconvolution for profile data consists in finding the coordinates  $(x_0, z_0)$  of the source center and a regional field  $B$  corresponding to the least-squares solution of

$$(x - x_0)f_x + (z - z_0)f_z = N(B - f), \quad x \in W, \quad (24)$$

where  $W = \{x_1, \dots, x_{NW}\}$  is a moving window that scans the profile. The Euler deconvolution algorithm does not require symmetric profiles for the dike model (Reid et al., 1990). Thus, it may be applied to the original profile or its reconstruction. As it will be seen later, the depth estimates from reconstructed and original profiles are similar, so one can infer that the reconstructed and original profiles are consistent. We use the structural index  $N=1$  and a moving window of  $NW=10$  points. Moreover, we select the solutions that satisfy the acceptance criterion  $z_0/(N\sigma_{z_0}) \geq 20$  (Thompson, 1982).

To cope with noisy data, we employ the integrated second vertical derivative (ISVD), which is more stable than the usual Fourier method (Fedi and Florio, 2001). Moreover, if local maxima of  $TAS_0$  and the special function  $S(x, z)$  are less than 100 m apart, only the highest one is retained.

The steps of the proposed decomposition are the following:

1. Calculate horizontal and vertical derivatives of the profile;
2. Evaluate the  $TAS_0$  (Eq. 18) and locate its minima;
3. For each pair  $[a_j, b_j]$  of adjacent minima of  $TAS_0$ :
  - 3.1. Estimate the effective dip angle  $Q_j$  using Equation 20;
  - 3.2. Calculate the reconstructed profile and its derivatives (Eqs. 15, 16, and 17);
4. Adjust the base level of  $f^{rec}$ :
  - 4.1. Compute the average value  $\overline{f^{rec}}$  of the reconstructed profile;
  - 4.2. For each pair  $[a_j, b_j]$  of adjacent minima of  $TAS_0$ :
    - 4.2.1. Define a straight line  $r_j$  from  $f^{rec}(a_j)$  to

$f^{rec}(b_j)$ ;

4.2.2. Subtract  $r_j$  from the reconstructed profile;

4.3. Add to the outcome of Step 4.2 the average value  $\overline{f^{rec}}$  from Step 4.1 to obtain the corrected profile.

## RESULTS AND DISCUSSION

In the following we test the reconstruction formula (Eq. 9), which we refer to as Hilbert Transform Decomposition (HTD), with examples of synthetic and field profiles generated by multiple dike-like structures. We obtain reconstructed profiles of the total field anomaly (TFA) and its vertical derivative (VDR). For field data, we also compare the HTD profiles with those obtained by reduction-to-the-pole (RTP).

### Synthetic examples

Let us consider a model of five dikes equally spaced by 500 m, whose coordinates of the centers and other parameters are indicated in Table 1. The dikes are illustrated in Figure 1. The sampling interval is 10 m. The magnetic anomalies are contaminated with standard Gaussian noise with a maximum noise amplitude equal 1% of the maximum anomaly amplitude. We consider the scenarios of the low and high variability of the effective dip angle  $Q$ , using the reconstruction formula given by Equations 14 and 15, respectively.

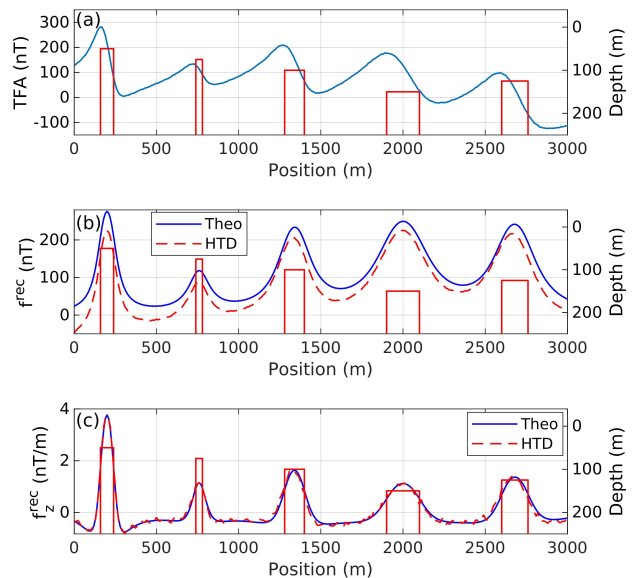


Figure 1: (a) Total field anomaly (TFA) generated by five dikes in the scenario of low variability of the effective dip angle (Table 1) contaminated by Gaussian noise of amplitude equal 1% of the data amplitude. (b) HTD reconstruction of the TFA. (c) HTD reconstruction of the VDR. The reconstructed profiles are compared with the noise-free symmetric part of the profile (Theo). For simplicity, the dikes are plotted with a vertical dip.

Table 1: Parameters of the model of five dikes. Two sets of effective dip angles are provided, to account for scenarios of low (\*) and high (\*\*) variability.

Parameter	Dike 1	Dike 2	Dike 3	Dike 4	Dike 5
Depth (m)	50	75	100	150	125
Half-width (m)	40	20	60	100	80
Amplitude (nT)	200	200	200	200	200
Coordinate of center (m)	200	760	1340	2000	2680
Effective dip angle (deg)*	-55	-60	-63	-58	-64
Effective dip angle (deg)**	-60	30	-10	60	90

In Figure 1 we present the noise-corrupted TFA (Figure 1a) and the reconstructed profiles (Figures 1b and 1c) in the scenario of low variability of  $Q$ . The reconstructed TFA profile obtained using Equation 14 is shifted to the theoretical, noise-free symmetric anomaly, as shown in Figure 1b, because the Hilbert transform needs to handle slow-decaying signals well (de Souza et al., 2020). On the other hand, the VDR decays more rapidly than the TFA and the reconstructed VDR obtained by HTD is better fitted to the theoretical one (Figure 1c). The effective dip angle obtained from Equation 20 was  $Q_{est} = -54.75^\circ$ , while the true average angle is  $Q = -60^\circ$  (see Table 1).

Let us now present the HTD reconstructed profile's use to estimate source depths from the profile shown in Figure 2a. The depth estimates based on the Signum-transform method using the original (TFA) and the reconstructed (HTD) profiles are presented in Figure 3a. The high discrepancy of the estimates obtained by TFA in Dike 5 (whose effective dip angle is  $90^\circ$ ) confirms that this method is sensitive to the magnetization direction and works better with symmetrical input data such as HTD. Figure 3b shows the depth estimates by Euler deconvolution using TFA and HTD profiles as in Figure 3a. The differences between the estimates using the original or the reconstructed profile are insignificant except for Dike 4, whose estimates are obtained only by TFA and are less accurate. The Signum-transform method provided accurate depths for all dikes, while Euler deconvolution tends to overestimate the depth of the deeper ones.

Let us proceed to the scenario of the high variability of  $Q$ . The TFA calculated in this scenario is shown in Figure 2a. In contrast, the reconstructed profiles are shown in Figures 2b and 2c. Except for the deeper dike (Dike 4), theoretical and HTD reconstructed anomalies are concordant.

Figure 4a compares the  $TAS_0$  with the analytic signal amplitude (ASA). Unlike ASA, the peaks of  $TAS_0$  have about the same amplitude, regardless of the depth of the source, hence are more clearly identifiable. We consider the local maxima of  $TAS_0$  corresponding to at least 80% of the absolute maximum and select each local minimum between two adjacent maxima. The approximate effective dip angles are illustrated in Figure 4b. Figure 4c illustrates the base-level adjustment of the reconstructed profile.

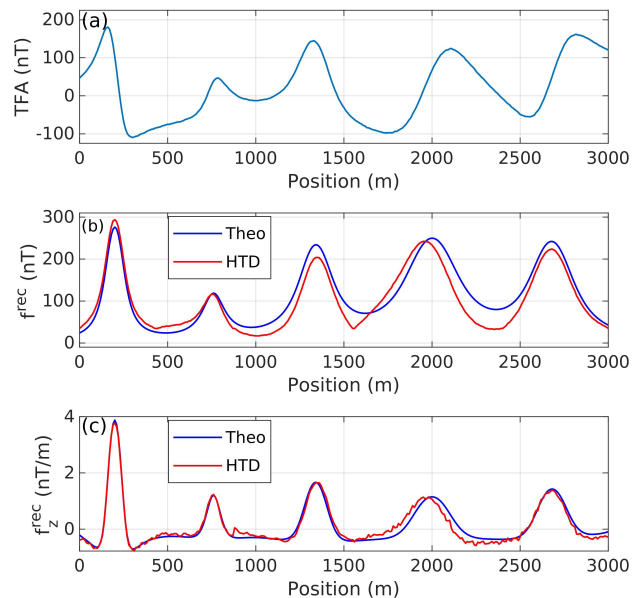


Figure 2: (a) Total field anomaly (TFA) generated by five dikes in the scenario of high variability of the effective dip angle (Table 1) contaminated by Gaussian noise of amplitude equal 1% of the data amplitude. (b) HTD reconstruction of the TFA. (c) HTD reconstruction of the VDR. The reconstructed profiles are compared with the noise-free symmetric part of the profile (Theo).

The last experiment concerns the influence of offset in the approximation of the effective dip angles (Table 2), reconstructed profiles (Figures 5 and 6), and depth estimates (Figures 7 and 8). The offsets between Dikes 2, 3, and 4 are successively increased from 100 m to 400 m. The reconstructed TFA is strongly affected by interference between sources.

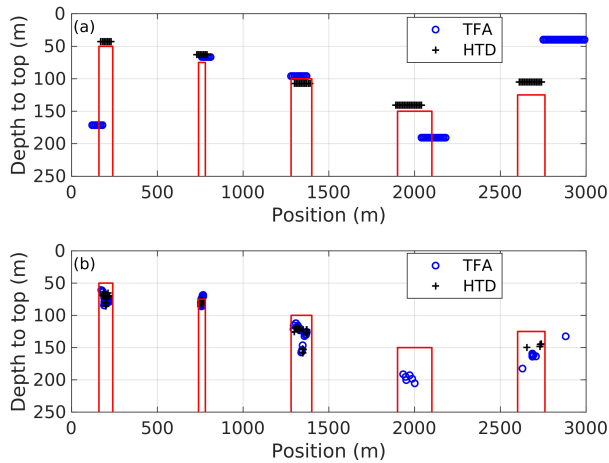


Figure 3: Depth estimates for the magnetic profile shown in Figure 2a: (a) Signum transform using the original (TFA) and reconstructed (HTD) profiles; (b) Euler deconvolution using TFA and HTD.

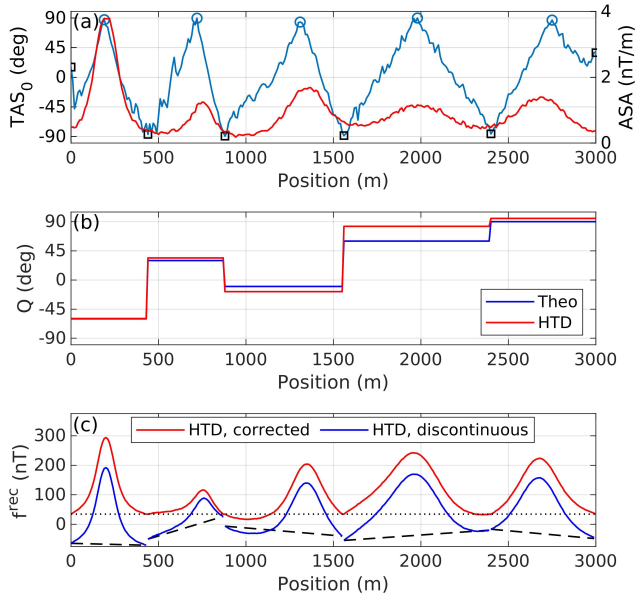


Figure 4: (a)  $TAS_0$  (blue) and ASA (red) of the data in Figure 2a. Circles and squares denote relative maxima and minima of  $TAS_0$ , respectively. (b) Effective dip angles estimated according to Equation 20 (red) and the exact angles (blue, see Table 1). (c) Base level adjustment of the reconstructed profile obtained from the data in Figure 2(a). The local base levels (dashed) are adjusted to the average value of the reconstructed profile (dotted).

The base levels at the central intervals are not appropriately determined (Figure 5). On the other hand, the anomalies are separated in the VDR, whose reconstructed profiles are accurate up to noise effects except when the offset is 100 m (Figure 6). These results suggest that our method may have a resolution limit of 100 m for dikes having about the same widths as in Table 1, which are intentionally more comprehensive for visualization purposes. Above this limit, depth estimates have shown to be robust concerning interference. Estimates from Signum transform using HTD, which depend on the reconstructed horizontal and vertical derivatives, are similar for all offsets on Dikes 1,2, and 5 (Figure 7). Estimates from Euler deconvolution (Figure 8) essentially follow the same pattern as in Figure 3b. Even though Euler deconvolution with HTD depends on the reconstructed TFA, which is affected by interference in the central part of the profile as shown in Figure 5, Euler solutions obtained by HTD have similar accuracy as those obtained with TFA (Figure 8). A possible explanation is that the inaccuracy in the base level will have more impact on the regional field parameter  $B$  (Eq. 24) than in the source location  $(x_0, z_0)$ .

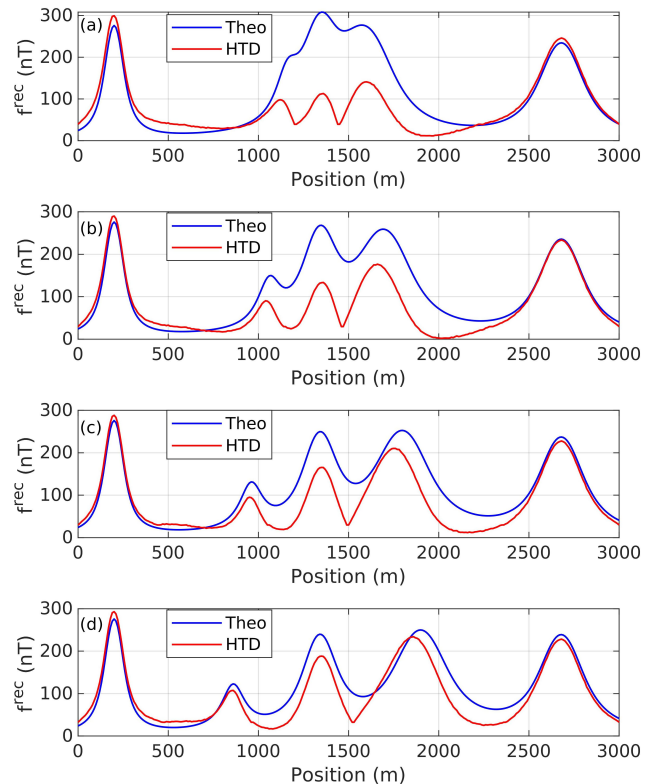


Figure 5: Theoretical (Theo) and HTD reconstructed profiles with offsets of 100 m (a), 200 m (b), 300 m (c), and 400 m (d) between Dikes 2, 3, and 4. The reconstructed profile with an offset of 500 m is shown in Figure 4a.

Table 2: Calculated effective dip angles in terms of the offset between Dikes 2, 3, and 4.

Dike	1	2	3	4	5
$Q$ (deg)	-60	30	-10	60	90
Offset (m)	$Q_{est}$ (deg)				
100	-56.75	88.00	-47.00	75.55	90.25
200	-56.75	55.25	-33.00	94.25	91.25
300	-58.75	37.25	-24.00	91.25	92.75
400	-58.25	35.25	-19.75	87.00	93.75
500	-59.50	34.00	-18.00	82.75	95.00

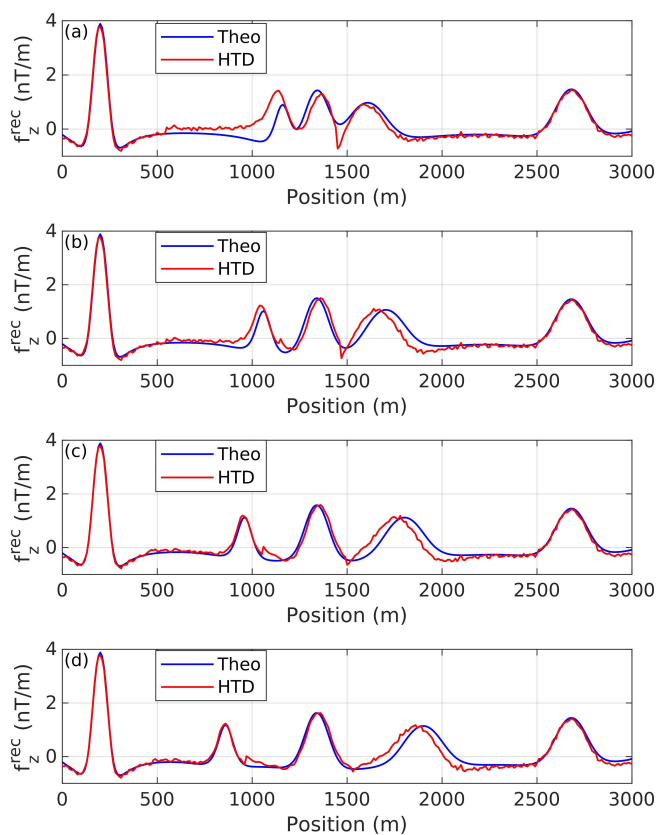


Figure 6: Theoretical (Theo) and HTD reconstructed VDR profiles with offsets of 100 m (a), 200 m (b), 300 m (c), and 400 m (d) between Dikes 2, 3, and 4. The reconstructed VDR with an offset of 500 m is shown in Figure 4b.

**Field example**

Our study area is located in the Ponta Grossa Arch (PGA), southern Brazil, which has been the subject of several recent studies (*e.g.*, Strugale et al., 2007; Gomes et al., 2011; Louro et al., 2019; Cavalcante et al., 2020).

A major feature of the PGA structural framework, presented by Ferreira (1982), is the presence of four magnetic lineaments, namely Guapiara (north-

ern limit), São Jerônimo-Curiúva and Rio Alonzo (central region), and Rio Piquiri (southern limit), as indicated in Figure 9. These lineaments extend over 600 km in the NW-SE direction and are related to diabase dike swarms.

We use a profile obtained from the ground magnetic survey by Castro et al. (2008). The profile is 12224 m long in the NE-SW direction, with a sampling interval of approximately 25 m. The geological map of the Ponta Grossa Arch and the location of the magnetic profile are indicated in Figure 9.

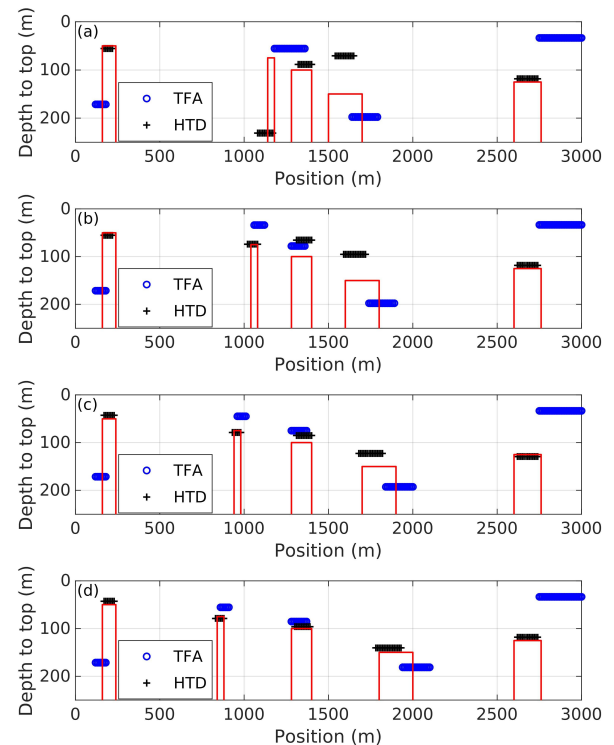


Figure 7: Depth estimates with Signum transform using the original (TFA) and reconstructed (HTD) profiles with offsets of 100 m (a), 200 m (b), 300 m (c), and 400 m (d) between Dikes 2, 3, and 4. Depth estimates with an offset of 500 m are shown in Figure 3a.

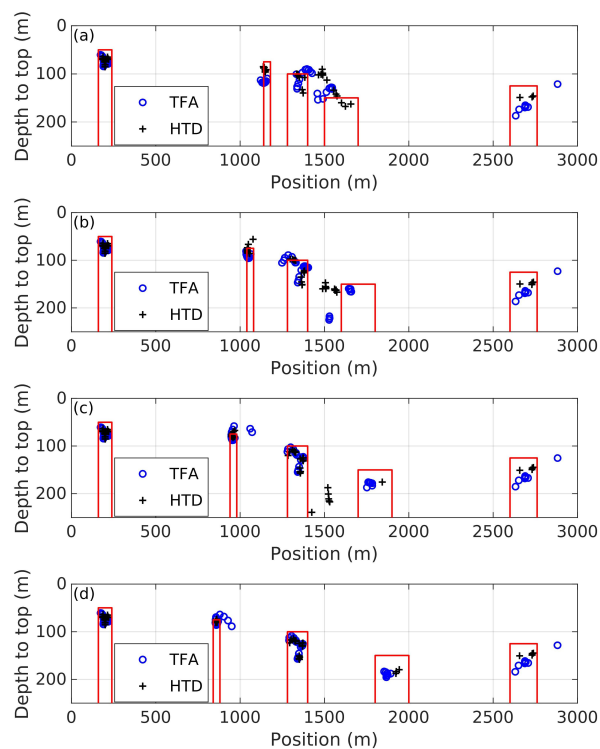


Figure 8: Depth estimates with Euler deconvolution using the original (TFA) and reconstructed (HTD) profiles with offsets of 100 m (a), 200 m (b), 300 m (c), and 400 m (d) between Dikes 2, 3, and 4. Depth estimates with an offset of 500 m are shown in Figure 3b.

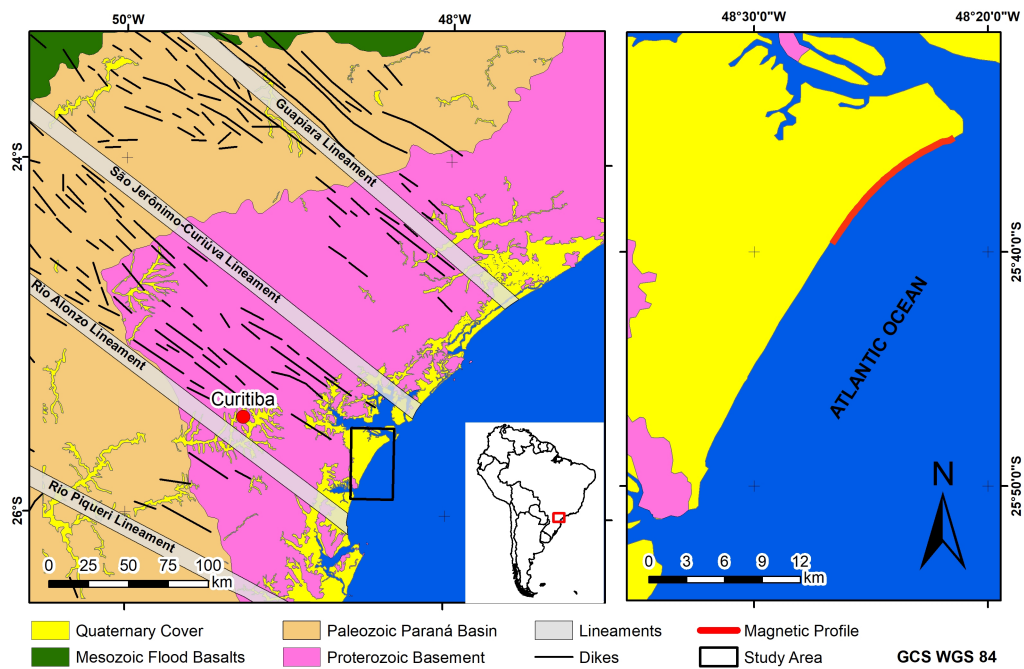


Figure 9: Simplified geological map of the Ponta Grossa Arch with the location of the study area (left) and the magnetic profile (right). Adapted from Louro et al. (2019).

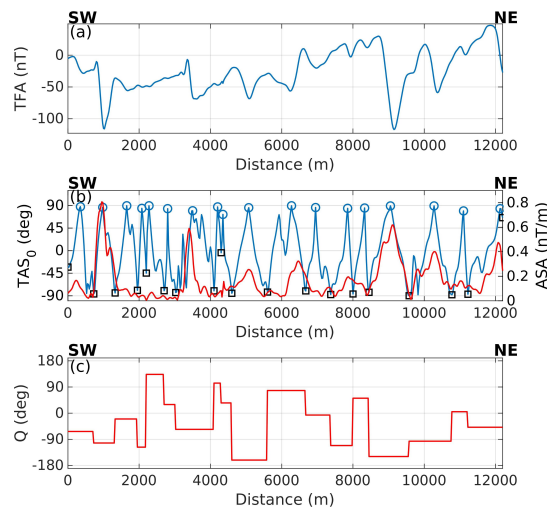


Figure 10: (a) TFA of the magnetic profile shown in Figure 9. (b)  $TAS_0$  (blue) and ASA (red) of the data in (a). Circles and squares denote relative maxima and minima of  $TAS_0$ , respectively. (c) Effective dip angles estimated according to Equation 20.

The profile data is shown in Figure 10a. As the synthetic example, we compute the  $TAS_0$  and the effective dip angle relative to this profile (Figures 10b and 10c, respectively). Figure 11 compares the results of HTD with those obtained using RTP, considering that during the acquisition the inclination and declination of the IGRF field were  $-35^\circ$  and  $-19^\circ$ , respectively (Castro et al., 2008). Figure 11a compares HTD and RTP transformations of TFA, while the comparisons of VDR are done in separate figures (Figures 11b and 11c). The ASA is displayed with the vertical derivatives to assess the independence from the effective magnetization direction.

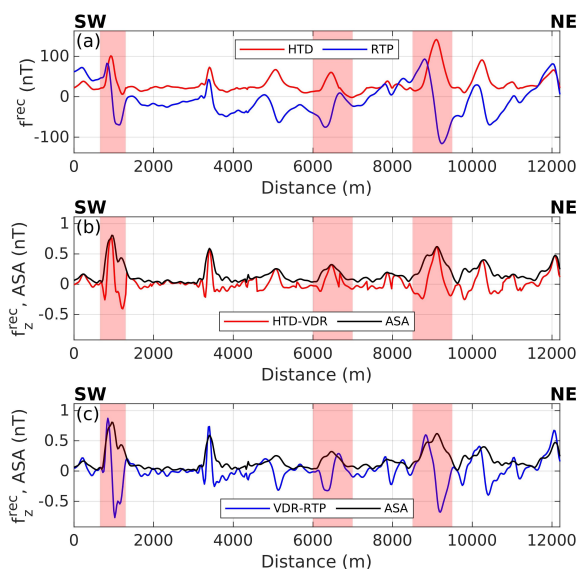


Figure 11: Reconstruction of the magnetic profile shown in Figure 9, compared with the RTP profile. (a) TFA (HTD and RTP). (b) HTD reconstruction of the VDR. (c) VDR of the RTP profile. In (b) and (c), the ASA (black line) is also shown. In the highlighted regions, RTP anomaly peaks are laterally displaced concerning ASA, unlike HTD.

In general, the reconstructed profiles obtained by HTD are in agreement with RTP profiles when remanent magnetization is not significant or has a direction similar to the induced one but the former can reduce the dipolarity due to remanence and/or geological dip while RTP is not capable to. Regarding vertical derivatives, most of the higher-amplitude anomaly peaks of the HTD curve coincide with those of the ASA curve (Figure 11b). Moreover, HTD provides a better resolution of small-amplitude anomalies than ASA. On the other hand, some peaks of the RTP anomalies are laterally displaced concerning ASA (highlighted regions in Figure 11c), indicating the presence of significant remanent magnetization in the sources of these anomalies.

In the following we present depth estimates obtained by the same methods considered in synthetic data. In addition to TFA or ASA, we also use RTP as input data. The estimates are superimposed on ASA, which approximately indicates the position of the sources.

Figure 12 shows the results from the Signum-transform method and Euler deconvolution. For the Signum-transform method, the depth estimates from TFA (Figure 12a) are displaced concerning the peaks of the ASA due to the influence of magnetization, considering that the Signum-transform method assumes  $Q = 0$ . In Figure 12c some depth estimates are displaced to a lesser extent as the RTP does not remove the influence of remanent magnetization. On the other hand, the solutions obtained by Signum transform using HTD (Figure 12b) are accurately located over the peaks of ASA. The Euler deconvolution solutions obtained by TFA (Figure 12a) are less clustered than those based on HTD and RTP (Figures 12b and 12c), especially around 9000 m. Nevertheless, the distribution of solutions on all approaches is similar, corroborating the low sensitivity of Euler deconvolution to the magnetization direction.

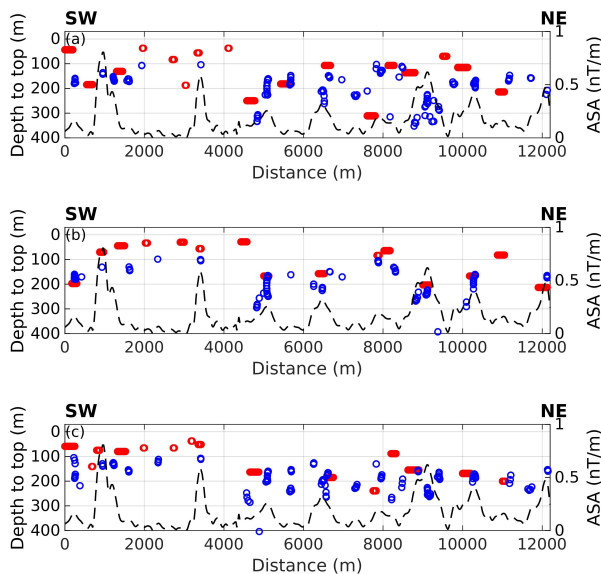


Figure 12: Depth estimates from the Signum-transform method (red) and Euler deconvolution (blue) for field data using (a) TFA (data from Figure 10a), (b) HTD (data from Figure 11a, red), and (c) RTP (data from Figure 11a, blue).

In general, the estimated depths obtained from Euler deconvolution using HTD as input are deeper than 100 m (Figure 12b). These estimates agree with the average thickness of sediment layers from three boreholes, located between 11 km and 21 km southwest of the study area, that reached the top of the basement between depths of 70 m and 100 m (Lessa et al., 2000). On the other hand, the Signum-transform method provides shallower solutions around 50 m (Figure 12b), between positions 0 m and 4000 m. Since the Signum-transform method has been more accurate in the synthetic data (Figure 3), we infer that the depth estimates from Signum transform are more reliable than those from Euler deconvolution also in field data.

## CONCLUSION

A new relationship between symmetric and antisymmetric components of a theoretical anomaly profile model was explored, leading to a reconstruction of the symmetric profile through an intuitive transformation of the zero-order analytic signal.

The proposed technique has produced symmetric reconstructed anomalies for synthetic and field data in the scenario of multiple dikes. The field example illustrates the main attributes of the reconstructed VDR: it yields narrower anomalies than the ASA, allowing more accurate location and identification of the sources, and it yields more symmetrical and centralized anomalies than RTP, because it is independent on the effective dip angle. The disadvantage of the method is that interference between sources poses difficulties to the reconstruction of TFA. We found in our experiments an offset limit of 100 m be-

tween dikes, which may change depending, *e.g.*, on their depths and widths. Below this value, the reconstructed profiles and depth estimates may need to be revised. However, some issues observed in the synthetic experiments, such as discontinuities between reconstructed anomalies, are barely seen in field data.

As an example of how HTD can improve existing methods, we combined it with the Signum-transform method for depth estimation. The sources' locations estimated by this approach were more consistent with ASA than the ones obtained by the Signum-transform method applied to RTP data. Compared with Euler deconvolution, the Signum-transform method has shown to be more accurate, as demonstrated in the synthetic example, in addition to being less spread out and more centered in both synthetic and real examples.

The low dependence of reconstructed profiles on magnetization facilitates forward and inverse modeling as the user does not have to account for remanence. The proposed technique could speed up the interpretation of profile data, as it does not require isolating a single anomaly or a preliminary investigation of remanent magnetism. These attributes can be helpful in the study of dike swarms, contributing to the understanding of the underlying tectonic processes.

## ACKNOWLEDGMENTS

The authors thank Associate Editor Alanna Costa Dutra and our anonymous reviewers for their careful evaluation of our manuscript. S. P. Oliveira and F. J. F. Ferreira are supported by CNPq under grants 316376/2021-3 and 303826/2018-5, respectively.

## REFERENCES

- Bastani, M., and L. B. Pedersen, 2001, Automatic interpretation of magnetic dike parameters using the analytical signal technique: *Geophysics*, **66**, 551–561, doi: [10.1190/1.1444946](https://doi.org/10.1190/1.1444946).
- Bhimasankaram, V. L. S., N. L. Mohan, and S. V. S. Rao, 1978, Interpretation of magnetic anomalies of dikes using Fourier transforms: *Geoexploration*, **16**, 259–266, doi: [10.1016/0016-7142\(78\)90015-7](https://doi.org/10.1016/0016-7142(78)90015-7).
- Castro, L. G., F. J. F. Ferreira, and R. J. Angulo, 2008, Modelo gravimétrico-magnético do gráben de Paranaguá-PR, Brasil: *Brazilian Journal of Geophysics*, **26**, 273–292, doi: [10.1590/S0102-261X2008000300002](https://doi.org/10.1590/S0102-261X2008000300002).
- Cavalcante, F. L., C. A. Mendonça, U. Ofterdinger, and O. A. de Souza Filho, 2020, Well productivity in the Ponta Grossa dike swarm, Brazil: An integrated study with magnetic data inversion and clustering analysis of model solutions: *Journal of Hydrology*, **588**, 125079, doi: [10.1016/j.jhydrol.2020.125079](https://doi.org/10.1016/j.jhydrol.2020.125079).
- Cooper, G. R. J., 2014, Reducing the dependence of the analytic signal amplitude of aeromagnetic

- data on the source vector direction: *Geophysics*, **79**, J55–J60, doi: [10.1190/geo2013-0319.1](https://doi.org/10.1190/geo2013-0319.1).
- Cooper, G. R. J., 2015, Using the analytic signal amplitude to determine the location and depth of thin dikes from magnetic data: *Geophysics*, **80**, J1–J6, doi: [10.1190/geo2014-0061.1](https://doi.org/10.1190/geo2014-0061.1).
- Cooper, G. R. J., and D. R. Cowan, 2006, Enhancing potential field data using filters based on the local phase: *Computers & Geosciences*, **32**, 1585–1591, doi: [10.1016/j.cageo.2006.02.016](https://doi.org/10.1016/j.cageo.2006.02.016).
- Dannemiller, N., and Y. Li, 2006, A new method for determination of magnetization direction: *Geophysics*, **71**, L69–L73, doi: [10.1190/1.2356116](https://doi.org/10.1190/1.2356116).
- de Souza, J., and F. J. F. Ferreira, 2012, On the use of derivatives for interpreting magnetic anomalies due to dyke-like bodies: Qualitative and quantitative analysis, in *Istanbul 2012 – International Geophysical Conference and Oil & Gas Exhibition: Society of Exploration Geophysicists*, 1–4. doi: [10.1190/IST092012-001.157](https://doi.org/10.1190/IST092012-001.157).
- de Souza, J., S. P. Oliveira, and F. J. F. Ferreira, 2020, Using parity decomposition for interpreting magnetic anomalies from dikes having arbitrary dip angles, induced and remanent magnetization: *Geophysics*, **85**, J51–J58, doi: [10.1190/GEO2019-0225.1](https://doi.org/10.1190/GEO2019-0225.1).
- Debeglia, N., and J. Corpel, 1997, Automatic 3-D interpretation of potential field data using analytic signal derivatives: *Geophysics*, **62**, 87–96, doi: [10.1190/1.1444149](https://doi.org/10.1190/1.1444149).
- Fedi, M., and G. Florio, 2001, Detection of potential fields source boundaries by enhanced horizontal derivative method: *Geophysical Prospecting*, **49**, 40–58, doi: [10.1046/j.1365-2478.2001.00235.x](https://doi.org/10.1046/j.1365-2478.2001.00235.x).
- Ferreira, F. J. F., 1982, Integração de dados aeromagnéticos e geológicos: configuração e evolução tectônica do Arco de Ponta Grossa: Master's thesis, University of São Paulo, Brazil.
- Gomes, C. B., E. Ruberti, P. Comin-Chiaramonti, and R. G. Azzone, 2011, Alkaline magmatism in the Ponta Grossa Arch, SE Brazil: a review: *Journal of South American Earth Sciences*, **32**, 152–168, doi: [10.1016/j.jsames.2011.05.003](https://doi.org/10.1016/j.jsames.2011.05.003).
- Hutchison, R. D., 1958, Magnetic analysis by logarithmic curves: *Geophysics*, **23**, 749–769, doi: [10.1190/1.1438525](https://doi.org/10.1190/1.1438525).
- Kara, I., O. T. Bal, A. B. Tekkeli, and G. Karcioğlu, 2017, A different method for interpretation of magnetic anomalies due to 2-D dipping dikes: *Acta Geophysica*, **65**, 237–242, doi: [10.1007/s11600-017-0019-8](https://doi.org/10.1007/s11600-017-0019-8).
- Lessa, G. C., R. J. Angulo, P. C. Giannini, and A. D. de Araujo, 2000, Stratigraphy and Holocene evolution of a regressive barrier in south Brazil: *Marine Geology*, **165**, 87–108, doi: [10.1016/S0025-3227\(99\)00130-9](https://doi.org/10.1016/S0025-3227(99)00130-9).
- Louro, V. H. A., A. P. Negrão, L. G. Castro, and F. J. F. Ferreira, 2019, Canoas geophysical anomaly: A possible alkaline body or unusual anomaly caused by mafic dykes in the Ponta Grossa Arch, Brazil?: *Journal of Applied Geophysics*, **170**, 103857, doi: [10.1016/j.jappgeo.2019.103857](https://doi.org/10.1016/j.jappgeo.2019.103857).
- McGrath, P. H., and P. J. Hood, 1970, The dipping dike case: A computer curve-matching method of magnetic interpretation: *Geophysics*, **35**, 831–848, doi: [10.1190/1.1440132](https://doi.org/10.1190/1.1440132).
- Mohan, N. L., N. Sundararajan, and S. V. Seshagiri Rao, 1982, Interpretation of some two-dimensional magnetic bodies using Hilbert transforms: *Geophysics*, **47**, 376–387, doi: [10.1190/1.1441342](https://doi.org/10.1190/1.1441342).
- Nabighian, M. N., 1972, The analytic signal of two-dimensional magnetic bodies with polygonal cross-section: its properties and use for automated anomaly interpretation: *Geophysics*, **37**, 507–517, doi: [10.1190/1.1440276](https://doi.org/10.1190/1.1440276).
- Naudy, H., 1971, Automatic determination of depth on aeromagnetic profiles: *Geophysics*, **36**, 717–722, doi: [10.1190/1.1440207](https://doi.org/10.1190/1.1440207).
- Oliveira, S. P., F. J. F. Ferreira, and J. de Souza, 2017, EdgeDetectPFI: an algorithm for automatic edge detection in potential field anomaly images – application to dike-like magnetic structures: *Computers & Geosciences*, **103**, 80–91, doi: .
- Paine, J., M. Haederle, and M. Flis, 2001, Using transformed TMI data to invert for remanently magnetised bodies: *Exploration Geophysics*, **32**, 238–242, doi: [10.1071/EG01238](https://doi.org/10.1071/EG01238).
- Phillips, J. D., R. O. Hansen, and R. J. Blakely, 2007, The use of curvature in potential-field interpretation: *Exploration Geophysics*, **38**, 111–119, doi: [10.1071/EG07014](https://doi.org/10.1071/EG07014).
- Pilkington, M., and M. Beiki, 2013, Mitigating remanent magnetization effects in magnetic data using the normalized source strength: *Geophysics*, **78**, J25–J32, doi: [10.1190/GEO2012-0225.1](https://doi.org/10.1190/GEO2012-0225.1).
- Powell, D. W., 1967, Fitting observed profiles to a magnetized dyke or fault-step model: *Geophysical Prospecting*, **15**, 208–220, doi: [10.1111/j.1365-2478.1967.tb01784.x](https://doi.org/10.1111/j.1365-2478.1967.tb01784.x).
- Ram Babu, H. V., and D. Atchuta Rao, 1991, Application of the Hilbert transform for gravity and magnetic interpretation: *Pure and Applied Geophysics*, **135**, 589–599, doi: [10.1007/BF01772408](https://doi.org/10.1007/BF01772408).
- Rao, B. S. R., and I. V. R. Murthy, 1967, Remanent magnetism of dykes and continental drift: *Pure and Applied Geophysics*, **68**, 124–130, doi: [10.1007/BF00874890](https://doi.org/10.1007/BF00874890).
- Reid, A. B., J. M. Allsop, H. Granser, A. J. Millett, and I. W. Somerton, 1990, Magnetic interpretation in three dimensions using Euler deconvolution: *Geophysics*, **55**, 80–91, doi: [10.1190/1.1442774](https://doi.org/10.1190/1.1442774).
- Roest, W. R., J. Verhoef, and M. Pilkington, 1992, Magnetic interpretation using the 3-D analytic signal: *Geophysics*, **57**, 116–125, doi: [10.1190/1.1443174](https://doi.org/10.1190/1.1443174).
- Salem, A., S. Williams, J. D. Fairhead, D. Ravat, and R. Smith, 2007, Tilt-depth method: A simple

- depth estimation method using first-order magnetic derivatives: *The Leading Edge*, **26**, 1502–1505, doi: [10.1190/1.2821934](https://doi.org/10.1190/1.2821934).
- Shuey, R. T., 1972, Application of Hilbert transforms to magnetic profiles: *Geophysics*, **37**, 1043–1045, doi: [10.1190/1.1440313](https://doi.org/10.1190/1.1440313).
- Strugale, M., S. P. Rostirolla, F. Mancini, C. V. Portela Filho, F. J. F. Ferreira, and R. C. de Freitas, 2007, Structural framework and Mesozoic–Cenozoic evolution of Ponta Grossa Arch, Paraná Basin, southern Brazil: *Journal of South American Earth Sciences*, **24**, 203–227, doi: [10.1016/j.jsames.2007.05.003](https://doi.org/10.1016/j.jsames.2007.05.003).
- Thompson, D. T., 1982, EULDPH: A new technique for making computer-assisted depth estimates from magnetic data: *Geophysics*, **47**, 31–37, doi: [10.1190/1.1441278](https://doi.org/10.1190/1.1441278).
- Weihermann, J. D., F. J. F. Ferreira, S. P. Oliveira, L. F. Cury, and J. de Souza, 2018, Magnetic interpretation of the Paranaguá terrane, southern Brazil by signum transform: *Journal of Applied Geophysics*, **154**, 116–127, doi: [10.1016/j.jappgeo.2018.05.001](https://doi.org/10.1016/j.jappgeo.2018.05.001).

**Oliveira, S. P.:** Conceptualization, methodology, editing and computer implementation; **de Souza, J.:** Conceptualization and methodology; **de Castro, L. G.:** Field data acquisition; **Ferreira, F. J. F.:** Conceptualization and methodology.

Received on November 14, 2022 / Accepted on March 24, 2023



Creative Commons attribution-type CC BY